# Large Effective-Strain Piezoelectric Actuators Using Nested Cellular Architecture With Exponential Strain Amplification Mechanisms

Jun Ueda, *Member, IEEE*, Thomas W. Secord, and H. Harry Asada, *Member, IEEE*

***Abstract*—Design and analysis of piezoelectric actuators having over 20% effective strain using an exponential strain amplification mechanism are presented in this paper. Piezoelectric ceramic material, such as lead zirconate titanate (PZT), has large stress and bandwidth, but its extremely small strain, i.e., only 0.1%, has been a major bottleneck for broad applications. This paper presents a new strain amplification design, called a "nested rhombus" multilayer mechanism, that increases strain exponentially through its hierarchical cellular structure. This allows for over 20% effective strain. In order to design the whole actuator structure, not only the compliance of piezoelectric material but also the compliance of the amplification structures needs to be taken into account. This paper addresses how the output force and displacement are attenuated by the compliance involved in the strain amplification mechanism through kinematic and static analysis. An insightful lumped parameter model is proposed to quantify the performance degradation and facilitate design tradeoffs. A prototype-nested PZT cellular actuator that weighs only 15 g has produced 21% effective strain (2.5 mm displacement from 12-mm actuator length and 30 mm width) and 1.7 N blocking force.**

***Index Terms*—Actuators, flexible structures, piezoelectric transducers.**

## I. Introduction

ACTUATORS play key roles in mechatronic and robotic devices. When a new robotics-related technology area emerges the demand for new actuation technologies strengthens. The authors have presented a unique "cellular actuator" concept, which in turn has a potential to be a novel approach to synthesize biologically inspired robot actuators [1]–[5]. The concept is to connect many small actuator units in series or in parallel, and compose in totality a macrosize linear actuator array similar to skeletal muscles. Promising applications include human assistive technologies [6]. In these applications, actuators are required to be fast, have zero backlash, be silent, energy efficient, and compact. Compliance may also be required for the sake of human safety. A large strain beyond 20% in actuation direction is desirable that is comparable with natural skeletal muscles [7]. It is expected that a large strain cellular actuator array can be used in a manner similar to biological muscles directly attached to skeletal structures. Another salient feature of the cellular actuator concept is modularity. The multitude of reconfigurable modular actuator units are connected in series and parallel to build various actuators with diverse stroke, force, and impedance characteristics. Simple ON–OFF controls [3], [4] will suffice to drive individual actuator units, since the aggregate outputs will be smooth and approximately continuous if a large number of modules are involved. ON–OFF controls are effective to overcome prominent hysteresis and nonlinearity of actuator materials [8]. Moreover, expensive analogue drive amplifiers are not required.

The basic module of this actuator array is a compact lead zirconate titanate (PZT) stack actuator. Piezoelectric ceramics, such as PZT, have a high power density, high bandwidth, and high efficiency. PZT outperforms other actuator materials, including shape memory alloy (SMA), conducting polymers, and electostrictive elastomers, with respect to speed of response and bandwidth. Its maximum stress is as large as SMA, and the efficiency is comparable to electrostrictive elastomers. Furthermore, PZT is a stable and reliable material that is usable in diverse, harsh environments. The most critical drawback of PZT is its extremely small strain, i.e., only 0.1%. Over the last several decades efforts have been taken to generate displacements out of PZT that are large enough to drive robotic and mechatronics systems [9]–[19]. These can be classified into: 1) inching motion or periodic wave generation; 2) bimetal-type bending; and 3) flextensional mechanisms. Inching motion provides infinite stroke and bimetal-type mechanism [18], [20] can produce large displacement and strain, applicable to various industrial applications when used as a single actuator unit; however, unfortunately, the reconfigurability by using these types may be limited due to the difficulty in arbitrarily connecting a large number of actuator units in series and/or in parallel to increase the total stroke and force, respectively. In contrast, flextensional mechanisms such as "Moonie" [9], [10], "Cymbal" [14], "Rainbow" [11], and others [16] are considered suitable for the reconfigurable cellular actuator design. An individual actuator can be stacked in series to increase the total displacement. Note that, this simple stacking also increases the length of the overall mechanism and does not improve the strain in actuation direction, which is known to be up to 2–3%.

In this paper, a new approach to amplifying PZT displacement will be presented [1], [2] to achieve over 20% effective strain. The key idea is hierarchical nested architecture that encloses

Manuscript received August 10, 2008; revised September 11, 2009; accepted September 21, 2009. Date of publication November 24, 2009; date of current version August 4, 2010. Recommended by Technical Editor G. Alici.

J. Ueda is with the George W. Woodruff School of Mechanical Engineering, Georgia Institute of Technology, Atlanta, GA 30332-0405 USA (e-mail: jun.ueda@me.gatech.edu).

T. W. Secord is with the Department of Mechanical Engineering, Massachusetts Institute of Technology, Cambridge, MA 02139 USA.

H. H. Asada is with the Brit and Alex d'Arbeloff Laboratory for Information Systems and Technology, Department of Mechanical Engineering, Massachusetts Institute of Technology, Cambridge, MA 02139 USA.

Color versions of one or more of the figures in this paper are available online at http://ieeexplore.ieee.org.

Digital Object Identifier 10.1109/TMECH.2009.2034973

smaller flextensional actuators with larger amplifying structures. A large amplification gain on the order of several hundreds can be obtained with this method. This structure is fundamentally different from traditional layered structures, such as telescoping cylindrical units [17] or stacking multiple plates connected by actuator wires [21]. Unlike these traditional stacking mechanism, where the gain $\alpha$ is proportional to the dimension of the lever or number of stacks, the amplification gain of the new mechanism increases exponentially as the number of layers increases. Suppose that strain is amplified $\alpha$ times at each layer of the hierarchical structure. For $K$ layers of hierarchical mechanism, the resultant gain is given by $\alpha^K$, the power of the number of layers. This nesting method allows us to gain a large strain in a compact body, appropriate for many robotic applications. This nesting approach may look rather straightforward; however, to the best of the authors' knowledge, there is no work that clearly formulated this exponential effect.

In the following, the design concept of exponential strain amplification with a nested structure will be presented, followed by an idealized force-displacement analysis and a feasibility study for achieving 20% strain using PZT stack actuators. A static lumped parameter model including mechanical compliance of the nested strain amplifier will be proposed to investigate how the forces and displacements generated by the individual PZT actuators are transmitted through the hierarchical mechanism, resulting in aggregate force and displacement at the output port. Design tradeoffs between the admissible and constrained motion spaces will be discussed based on the insightful lumped model. The lumped parameter model of lower layers can be recursively nested into a higher lumped parameter model to evaluate complex nested mechanisms without developing a full numerical model such as finite element method (FEM) [22]. The validity of the proposed concept will be confirmed through the design of a prototype actuator producing a displacement of 2.53 mm from 12-mm actuator length, which is equivalent to 21% effective strain, 30 mm of width, 1.69 N of blocking force, and 15 g of body mass.

## II. Exponential Strain Amplification Using Nested Rhombus Mechanisms

### A. Preliminary Kinematic Analysis of Flextensional Mechanisms and Effective Strain

This section briefly describes the kinematics of traditional "Moonie" flextensional mechanisms [9] that will be used for the basis of our proposed "nested rhombus" multilayer mechanism. As shown in Fig. 1(a), the main part of the mechanism is a rhombus-like hexagon that contracts vertically as the internal unit shown in grey expands. The vertical displacement, that is, the output of the mechanism, is amplified if the angle of the oblique beams to the horizontal line is less than $45^\circ$. Fig. 1(b) illustrates how the strain is amplified with this mechanism. Let $h_1$, $w_1$, and $\epsilon_0$ be, respectively, the height, width, and strain of the internal unit. Also let $d_1$ be the initial gap between the surface of the internal unit and the apex of the rhombus mechanism. In this section, it is assumed that all the joints are purely rotational and that all the beams are completely rigid. Also assume that

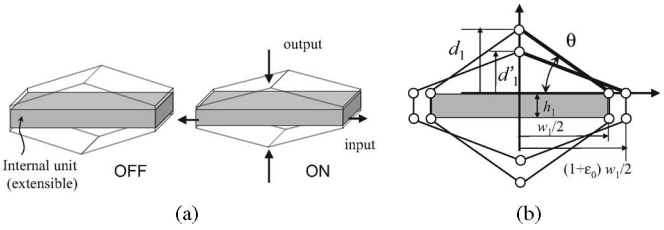


Fig. 1. Amplification principle of flextensional mechanisms [9]. (a) Actuation of flextensional mechanism. (b) Amplification of effective strain.

the internal unit is extensible; it can be extended to a contractive case with minor changes to the following formulation. As the internal unit, e.g., a PZT stack actuator, expands, the gap $d_1$ contracts to $d'_1$

$$d'_1 = \sqrt{\frac{d_1^2 - (\epsilon_0^2 + 2\epsilon_0) w_1^2}{4}}. \tag{1}$$

Then, the amplification gain $a_1$ of the displacement is given by

$$a_1 = \frac{2\Delta x_1}{\epsilon_0 w_1} \tag{2}$$

where $\Delta x_1 \triangleq d_1 - d'_1$. For small $\epsilon_0$, this can be approximated to $a_1 = w_1/2d_1 = \cot\theta$, where $\theta$ is the angle of the oblique beam to the horizontal line, as shown in the figure. Note that, this instantaneous amplification gain does not apply to large strain because of the nonlinearity in (1). A smaller value for the angle of the oblique beams $\theta$ gives a larger amplification gain. However, the angle $\theta$ needs to be carefully determined to avoid buckling of the beams due to unexpected external forces. As will be explained the later section, buckling of the beams cannot be neglected in the mechanical design since the working direction alternates from layer to layer in the proposed nested structure. Typically, this amplification gain alone can increase displacement to only three to five times larger.

The initial length of the rhombus mechanism measures $2d_1 + h_1$ along the output axis. Since the displacement created in this output direction is $2\Delta x_1$, the "effective strain" along the output axis can be defined as

$$\epsilon_1 \triangleq \frac{2|\Delta x_1|}{2d_1 + h_1}. \tag{3}$$

Note that the lateral size, perpendicular to the output direction, is not included in the definition of the effective strain. Comparing this to the input strain, $\epsilon_0$ yields the strain amplification gain given by

$$\alpha_1 \triangleq \frac{\epsilon_1}{\epsilon_0} = a_1 \frac{w_1}{2d_1 + h_1} \tag{4}$$

where $w_1/(2d_1 + h_1)$ is the ratio of the width to the height of the rhombus, i.e., the aspect ratio of the mechanism. Note that both the displacement amplification and the aspect ratio of the mechanism contribute to the resultant strain amplification $\alpha_1$. Strictly speaking, the aspect ratio is not a strain amplifier. However, since: 1) the effective strain amplification is defined to be the ratio of output displacement to the natural body length in the same direction as the output and 2) the direction of

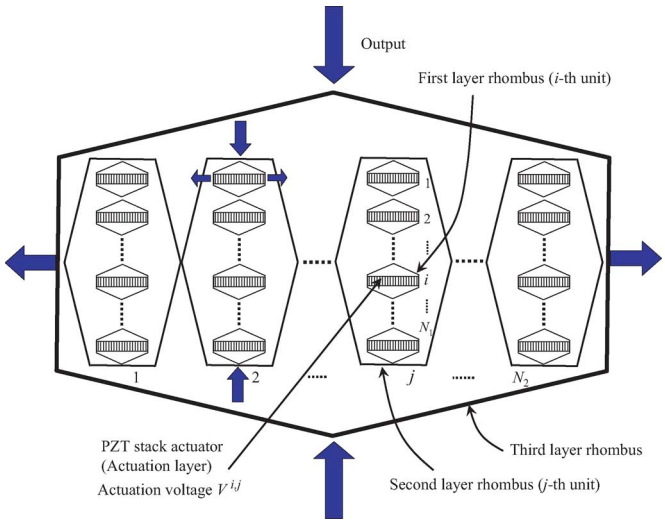


Fig. 2. Proposed nested structure for exponential strain amplification: The strain is amplified by three layers of rhombus strain amplification mechanisms, with the first layer, called an actuator layer, consisting of the smallest rhombi directly attached to the individual PZT stack actuators.

input strain and that of the output displacement are perpendicular to each other, the effective gain $\alpha_1$ is apparently amplified by the aspect ratio. Increasing the aspect ratio increases the strain amplification gain $\alpha_1$. However, space constraints must be considered since a larger aspect ratio increases the lateral size of the actuator that would affect on force capacity.

### B. Nested Rhombus Structure

The aforementioned mechanism for amplifying small displacements of PZT actuators have already been developed both in macroscale [9] and microscale [19] and have been applied to commercial products [23]. Our method is to extend this technique to: 1) gain an order-of-magnitude larger strain amplification; and 2) build a modular structure that is flexible and extensible.

Fig. 2 illustrates a new mechanism, called a "nested rhombus" strain amplifier, which consists of the multitude of rhombus mechanisms arranged in a hierarchical structure. The innermost unit, i.e., the building block of the hierarchical system, is the standard rhombus mechanism, or conventional flextensional mechanism, described previously. These units are connected in series to increase the output displacement. Also these units can be arranged in parallel to increase the output force. The salient feature of this hierarchical mechanism is that these rhombus units are enclosed with a larger rhombus mechanism that amplifies the total displacement of the smaller rhombus units. These larger rhombus units are connected together and enclosed with an even larger rhombus structure to further amplify the total displacement. Note that the working direction alternates from layer to layer; e.g., the second layer rhombus extends when the inner-most first layer units contract as shown in Fig. 1(b).

As this enclosure and amplification process is repeated, a multilayer strain-amplification mechanism is constructed, and the resultant displacement increases exponentially. Let $K$ be

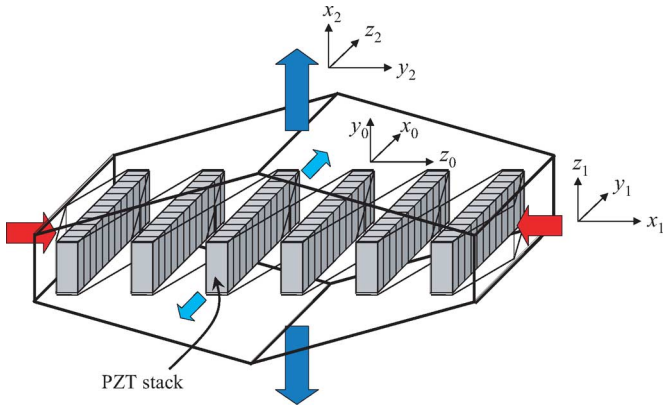


Fig. 3. 3-D nesting for 20% strain.

the number of amplification layers. Assuming that each layer amplifies the strain $\alpha$ times, the resultant amplification gain is given by $\alpha$ to the *power* of $K$

$$\alpha_{\text{total}} = \alpha^K. \tag{5}$$

For $\alpha = 15$, the gain becomes $\alpha_{\text{total}} = 225$ by nesting two rhombus layers and $\alpha_{\text{total}} = 3375$ with three rhombus layers. The nested rhombus mechanism with this hierarchical structure is a powerful tool for gaining an order-of-magnitude larger amplification of strain. As described before, our immediate goal is to produce 20% strain. This goal can be accomplished with $\alpha = 15$ and $K = 2$: $0.1\% \times 15 \times 15 = 22.5\%$.

This nested rhombus mechanism has a number of variations, depending on the numbers of serial and parallel units arranged in each layer and the effective gain in each layer. In general, the resultant amplification gain is given by the multiplication of each layer gain $\alpha_{\text{total}} = \prod_{k=1}^{K} \alpha_k$, where $\alpha_k \triangleq \epsilon_k / \epsilon_{k-1}$ is the $k$th layer's effective gain of strain amplification computed recursively with the following formula:

$$\epsilon_k = \frac{2d_k - \sqrt{4d_k^2 - (\epsilon_{k-1}^2 + 2\epsilon_{k-1})w_k^2}}{2d_k + h_k}, \quad k = 1, \ldots, K. \tag{6}$$

Another important feature of the nested rhombus mechanism is that two planes of rhombi in different layers may be arranged perpendicular to each other. This allows us to construct 3-D structures with diverse configurations. For simplicity, the schematic diagram in Fig. 2 shows only a 2-D configuration, but the actual mechanism is three-dimensional, with output axes being perpendicular to the plane. 3-D arrangement of nested rhombus mechanisms allows us to densely enclose many rhombus units in a limited space. For example, Fig. 3 illustrates a 3-D structure. Note that, the serially connected first-layer rhombus units are rotated $90^\circ$ about their output axis $x_1$. This makes the rhombus mechanism at the second layer more compact; the length in the $x_2$ direction is reduced. Namely, the height $h_1$ in Fig. 1(b), which is a nonfunctional dimension for strain amplification, can be reduced. These size reductions allow us not only to pack many PZT units densely but also increase the effective strain along the output axis $\epsilon_1$, since $h_1$ is involved in the denominator of (3).

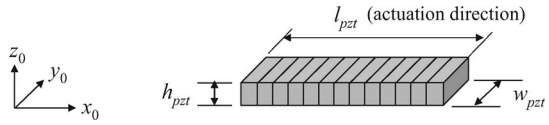


Fig. 4. Actuator coordinate system of PZT stack actuator.

## III. Properties of Ideal Nested Rhombus PZT Actuators

### A. Aggregate Force and Displacement

In the nested rhombus PZT actuator, displacements of the individual PZT actuators are aggregated and transmitted through the multiple layers of strain amplification mechanisms, resulting in an output displacement at the final layer. Similarly, the output force is the resultant force of many PZT actuators. In this section, these aggregate force and displacement are analyzed in relation to the individual PZT actuator outputs based on an ideal kinematic and static model of the nested rhombus mechanism.

Consider a PZT stack actuator shown in Fig. 4. Let $l_{\rm PZT}$, $w_{\rm PZT}$, and $h_{\rm PZT}$ be the length, width, and height of a PZT stack actuator, respectively. The $x$-axis is defined as the actuation direction. Choice of $y$ and $z$ axes is arbitrary. For descriptive purposes, the $y$-axis is chosen to the direction of $w_{\rm PZT}$ as shown in Fig. 4. The displacement of this PZT stack actuator when no load is connected to the actuator is given by

$$\Delta x_{\rm PZT} = N_{\rm film} d_{33} V \tag{7}$$

where $N_{\rm film}$ is the number of PZT films along the actuation direction, $d_{33}$ is piezoelectric coefficient, and $V(>0)$ is voltage applied to each PZT film. Strictly speaking, the piezoelectric coefficient $d_{33}$ is not a constant; according to [24] it may vary significantly as strain gets larger. In this paper, however, it is assumed to be constant. The inherent stiffness of this actuator is given by $k_{\rm PZT} = E_{\rm PZT} h_{\rm PZT} w_{\rm PZT} / l_{\rm PZT}$,where $E_{\rm PZT}$ is the elastic modulus of PZT material.

The no-load displacement given by (7) results from the balance between the net force $f_{\rm PZT}$ produced by the PZT and the restoring force due to the stiffness $k_{\rm PZT}$, which is proportional to $\Delta x_{\rm PZT}$. Unlike standard electromagnetic actuators, e.g., dc and ac motors, PZT and other actuator materials cannot produce force independent of its displacement. Due to the inherent structural stiffness the net output force of these actuator materials gets substantially lower when producing a displacement at the same time.

Consider the following force–displacement relationship; the force generated by the PZT stack actuator while producing displacement $\Delta x_{\rm PZT}$ is given by

$$f_{\rm PZT} = k_{\rm PZT}(\beta V - \Delta x_{\rm PZT}) \tag{8}$$

where $\beta = N_{\rm film} d_{33}$. As this PZT stack is imbedded in a first rhombus mechanism, the force is reduced to $1/a_1$ and the displacement is amplified $a_1$ times, i.e., $f_1 = f_{\rm PZT}/a_1$ and $\Delta x_1 = a_1 \Delta x_{\rm PZT}$. Assuming that the rhombus mechanism is loss-less and that the beams are completely rigid and are connected with free joints, the force–displacement relationship at the output axis of the first layer rhombus mechanism is given by

$$f_1 = \frac{f_{\rm PZT}}{a_1} = \frac{k_{\rm PZT}}{a_1}\beta V - \frac{k_{\rm PZT}}{(a_1)^2}\Delta x_1. \tag{9}$$

Note that, the equivalent stiffness of the PZT stack viewed from the output side of the rhombus mechanism is attenuated by a factor of $1/(a_1)^2$.

Suppose that $N_1$ units of this first layer are connected in series and are enclosed with a second-layer mechanism. Each unit is numbered from 1 to $N_1$. Parallel connection in a layer is not considered since it forms a closed kinematic chain for ideal rhombus mechanisms and solving the kinematic chain problem is not essential. Let $V^i$, $f_1^i$, and $\Delta x_1^i$ $(i = 1, \ldots, N_1)$, respectively, be the voltage, force, and displacement of the $i$th unit in the serial connection of the first layers. The force is common to all the $N_1$ units

$$f_1^1 = f_1^2 = \cdots = f_1^{N_1} \triangleq f_1^{\rm com}. \tag{10}$$

From (9), we have

$$\frac{k_{\rm PZT}}{a_1}\beta V^i - \frac{k_{\rm PZT}}{(a_1)^2}\Delta x_1^i = f_1^{\rm com}, \quad (i = 1, \cdots, N_1). \tag{11}$$

Suppose that, the second rhombus mechanism amplifies displacement and attenuates force $a_2$ times. The resultant displacement at this layer is given by

$$\Delta x_1^1 + \cdots + \Delta x_1^{N_1} = \frac{\Delta x_2}{a_2}. \tag{12}$$

From (11) and (12), the relationship between the output force and displacement for the second layer is given by

$$f_2 = \frac{f_1^{\rm com}}{a_2} = \frac{\beta k_{\rm PZT}}{N_1 a_1 a_2}\sum_{i=1}^{N_1} V^i - \frac{k_{\rm PZT}}{N_1 (a_1)^2 (a_2)^2}\Delta x_2. \tag{13}$$

Repeating the same process yields the relation between the aggregate displacement and force along the $K$th layer output axis

$$f_K = \frac{\beta k_{\rm PZT}}{\prod_{k=1}^{K} a_k}\frac{1}{\prod_{k=1}^{K-1} N_k}\sum_{1}^{N_{K-1}}\cdots\sum_{j=1}^{N_2}\sum_{i=1}^{N_1} V^{i,j,\ldots} - \frac{k_{\rm PZT}}{\prod_{k=1}^{K-1} N_k \prod_{k=1}^{K} (a_k)^2}\Delta x_K. \tag{14}$$

Totally, $N_{K-1}, N_{K-2}, \ldots, N_1$ PZT units are involved in the system, and $V^{i,j,\cdots}$ in the aforementioned equation represents the voltage applied to each individual PZT actuator. See Fig. 2 for $K = 3$, where $V^{i,j}$ is applied to the $i$th PZT unit in the first layer involved in the $j$th unit $(j = 1, \ldots, N_2)$ of the second layer.

From the aforementioned results we can note that the following points.

1) Given applied voltages, the maximum of the aggregate displacement is obtained when no force is generated, i.e., free load. This aggregate free-load displacement $\Delta x_K^{\rm free}$ is proportional to the total sum of the inputs $\sum_1^{N_{K-1}}\cdots\sum_1^{N_2}\sum_1^{N_1} V^{i,j,\cdots}$ amplified by a factor of $\prod_{k=1}^{K} a_k$.

2) The maximum of the aggregate force is obtained when the output displacement is totally blocked. This aggregate blocking

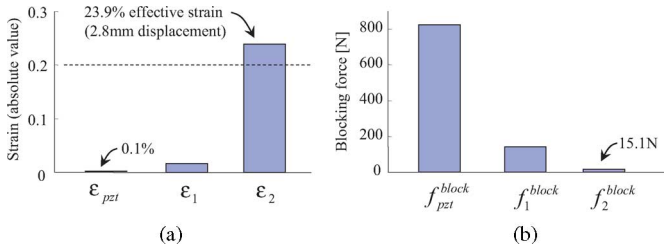


Fig. 5. Idealized analysis: compliance of the amplification mechanism is not considered. (a) Strain (without load). (b) Blocking force.

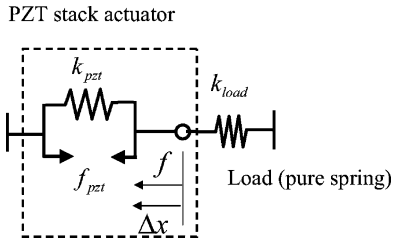


Fig. 6. Model of PZT stack actuator connected to a spring load.

force $f_K^{\text{block}}$ is proportional to the average of the entire inputs: $\frac{1}{\prod_{k=1}^{K-1} N_k} \sum_1^{N_{K-1}} \cdots \sum_1^{N_2} \sum_1^{N_1} V^{i,j,\ldots}$.

If the total number of PZT actuators is very large, the individual PZT stack actuators can be driven with simple ON–OFF controls [3], [4], since the net effect upon the output displacement and force is the summation and average of many PZT actuators. Expensive analogue drivers and controllers are unnecessary for the cellular actuators. As the number of PZT actuator units increases, discretization error becomes small and smooth output displacement and force can be expected.

### B. Feasibility Check for 20% Strain

Fig. 3 also illustrates a design example aiming at 20% effective strain. In this design example, six first-layer rhombus units are connected in series. As described in the previous section, 3-D structure plays a key role for large strain. The serially connected units are rotated $90^\circ$ and inserted into the second layer rhombus. By this design, the second layer rhombus extends when the PZT stack actuators are turned ON, since they are extensible and the number of amplifying layers is 2.

Let the size of the PZT stack actuator be 12.8 mm ($l_{\text{PZT}}$) $\times$ 6 mm ($w_{\text{PZT}}$) $\times$ 2.5 mm ($h_{\text{PZT}}$). The initial gap $d_1$ between the surface of the PZT stack actuator and the apex of the first rhombus mechanism is 1.1 mm. We apply typical values of PZT-ceramics for Young's modulus and strain, i.e., $E_{\text{PZT}} = 55.0$ GPa, and $\epsilon_{\text{PZT}} (= \epsilon_0) = 0.1\%$. These dimensional parameters have been determined according to a commercially available PZT actuator, Cedrat APA50XS [23], as the first layer unit. The size of the second layer is 12.0 mm (length, actuation direction) $\times$ 28.2 mm (width) $\times$ 12.8 mm (height). The thicknesses of the amplifying mechanisms and connection parts between the units have been neglected for simplicity.

From iterative calculations of (9) and (13), the amplified strain and reduced blocking force are obtained as shown in Fig. 5. The prospective displacement is 2.8 mm for the actuator length of 12 mm, which is equivalent to $\epsilon_2 = 23.9\%$. This result implies that over 20% stain is feasible by the proposed nested structure. Also, the resultant blocking force is predicted to be 15.1 N.

## IV. Nested Rhombus Mechanisms with Structure Flexibility

The aforementioned initial design was conducted based on the ideal kinematic model having rigid beams and free joints at the strain amplification mechanism. Actual mechanisms, however, inevitably have some compliance at the structure, which may degrade the aggregate force and displacement. Not only the compliance of piezoelectric stack actuators but also the compliance of the amplification structures need to be taken into account in designing the nested strain amplification mechanism to minimize its adverse effect.

In this paper, we focus on static analysis in order to better understand physical limitations and design tradeoffs of the nested rhombus mechanisms. Meeting a static performance goal is the primary concern in designing a strain amplifier of this kind. Dynamic analysis and synthesis will be reported in a companion paper [25]. We assume that the linear characteristic in (8) holds for simplicity since the hysteresis compensation of piezoelectric materials has long been studied [26] and is not the main aim of this paper.

### A. Effects of Joint Stiffness and Beam Compliance

Consider a spring load serially connected to a PZT stack actuator, as shown in Fig. 6. Let $k_{\text{load}}$ be a spring constant of the load, and $\Delta x_{\text{PZT}}$ be the displacement of the load. The following equations hold:

$$f_{\text{PZT}} = (k_{\text{load}} + k_{\text{PZT}}) \Delta x_{\text{PZT}} \tag{15}$$

$$f = k_{\text{load}} \Delta x_{\text{PZT}} \tag{16}$$

where $f$ is the actuator output force applied to the load. The free-load displacement $\Delta x_{\text{PZT}}^{\text{free}}$ is calculated by letting $k_{\text{load}} = 0$.

Eliminating $\Delta x_{\text{PZT}}$ yields

$$f = \frac{k_{\text{load}}}{k_{\text{PZT}} + k_{\text{load}}} f_{\text{PZT}}. \tag{17}$$

Note that, the actuator output force $f$ becomes significantly lower than the original PZT force $f_{\text{PZT}}$ when $k_{\text{PZT}}$ gets larger or $k_{\text{load}}$ gets lower. Similarly, the output displacement $\Delta x_{\text{PZT}}$ also gets attenuated

$$\Delta x_{\text{PZT}} = \frac{k_{\text{PZT}}}{k_{\text{PZT}} + k_{\text{load}}} \Delta x_{\text{PZT}}^{\text{free}}. \tag{18}$$

The simple model described here shows that both output force and displacement are attenuated due to the compliance of the connected load as well as the stiffness of the actuator itself. When this PZT stack actuator is connected to a rhombus strain amplification mechanism, an external load having properties similar to the aforementioned $k_{\text{load}}$ and $k_{\text{PZT}}$ will be imposed on the PZT actuator. As many layers of the amplification mechanism are attached to the PZT stack actuator, these structural

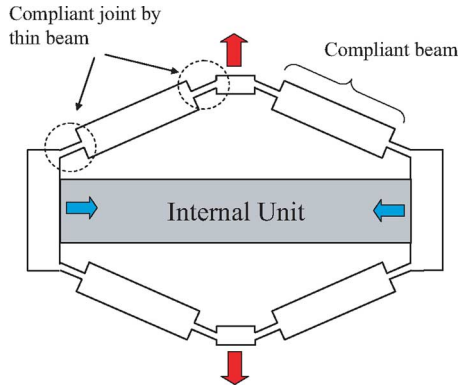


Fig. 7. Embodiment of rhombus mechanism.

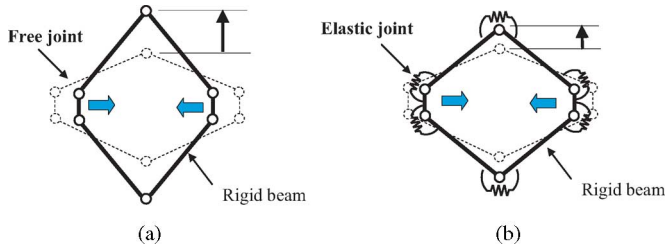


Fig. 8. Effect of joint compliance on free-load displacement. (a) Ideal rhombus. (b) Rhombus with elastic joints.

effects will be even more prominent. In the ideal mechanism shown in Fig. 1(b), we have assumed that the four beams of the rhombus are completely rigid and that all the joints are free to rotate and purely revolving. However, these assumptions do not hold in real structures.

Note that fabrication of free joints is difficult in small scale due to mechanical tolerance and play. For the first and second layers, in particular, where the displacement is extremely small, the displacement created by the PZT is likely to diminish due to play at the joints. Therefore, flexural pivots and flexible beams [16], [19], [23] have been used for amplifying PZT displacement. Fig. 7 shows an example embodiment of the rhombus mechanism. These flexural joints and beams inevitably bring undesirable properties to the system. There are three types of undesirable properties as mentioned in the following points.

1) First, the joints are no longer free joints, but they impose a spring load that the PZT has to overcome. Fig. 8 depicts this parasitic effect of joint stiffness; some fraction of the PZT force is wasted for coping with the joint stiffness. This results in reduction in free-load displacement. This implies that the joint stiffness has an equivalent effect to that of the PZT stiffness $k_{\mathrm{PZT}}$ in Fig. 6. The stiffness of the joints brings increased stiffness $k_{\mathrm{PZT}}$ for the PZT to overcome.

2) Second, flexibility at the beams may attenuate the displacement and force created by the PZT. Consider the case where the output displacement is blocked as shown in Fig. 9. As the PZT generates a displacement, the beams are deformed and thereby the transmitted force becomes lower; at least it does not reach the same level as that of the rigid beams. Similarly, if the output axis is coupled to another compliant load, the output force and

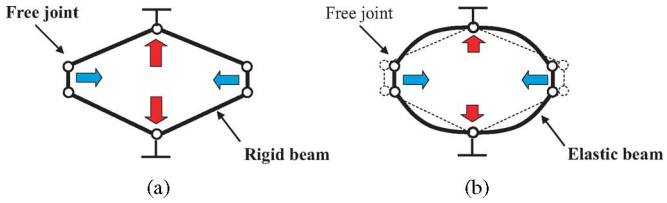


Fig. 9. Effect of beam compliance on blocking force. (a) Ideal rhombus. (b) Rhombus with elastic beams.

displacement will be prorated between the load compliance and the beam compliance. As the beam stiffness becomes lower, the output force and displacement decrease.

3) Third, flexural joints not only create pure rotational displacements but also often cause unwanted translational displacements. These elastic deformations at the joint along the direction of the beam incur the same problem as the beam compliance; the force and displacement created by the PZT tend to diminish at the joints.

It is important to distinguish two different types of compliance in the aforementioned cases: One is to take place in the kinematically admissible space of the ideal rhombus mechanism, and the other is in the orthogonal complement to the former, termed the constrained space [27]. The joint stiffness described in 1) is in the admissible motion space, while 2) and 3) are in the constrained space. Curved beams, such as seen in Moonies, contain compliance in both constrained and admissible spaces. The distributed compliance can be approximated into the two types of lumped compliant elements. To minimize the adverse effects of the nested rhombus mechanism, the stiffness in the admissible space must be minimized and the stiffness in the constrained space must be maximized. As multiple layers of strain amplification mechanisms are used, the compliances in the admissible and constrained spaces become more intricate. In the following sections, the kinematic and static characteristics of multilayer compliant rhombus mechanisms will be analyzed.

### *B. Modeling of Single-Layer Flexible Rhombus Mechanisms*

Consider the case shown in Fig. 10(a) where a rhombus mechanism, including Moonies, is connected to a spring load. $k_{\mathrm{load}}$ is an elastic modulus of the load, and $k_{\mathrm{PZT}}$ is an elastic modulus of the internal unit such as a PZT stack actuator. $\Delta x_{\mathrm{PZT}}$ is the displacement of the internal unit, and $f_{\mathrm{PZT}}$ is the force applied to the amplification mechanism from the internal unit. $f_1$ is the force applied to the load from the actuator, and $\Delta x_1$ is the displacement of the load. In this figure, we assume that the internal unit is contractive for later convenience.

The rhombus strain amplification mechanism is a two-port compliance element, whose constitutive law is defined by a $2 \times 2$ stiffness matrix

$$\begin{bmatrix} f_I \\ f_O \end{bmatrix} = \boldsymbol{S} \begin{bmatrix} \Delta x_{\mathrm{PZT}} \\ \Delta x_1 \end{bmatrix} \tag{19}$$

where

$$S^{2\times 2} = \begin{bmatrix} s_1 & s_3 \\ s_3 & s_2 \end{bmatrix}$$

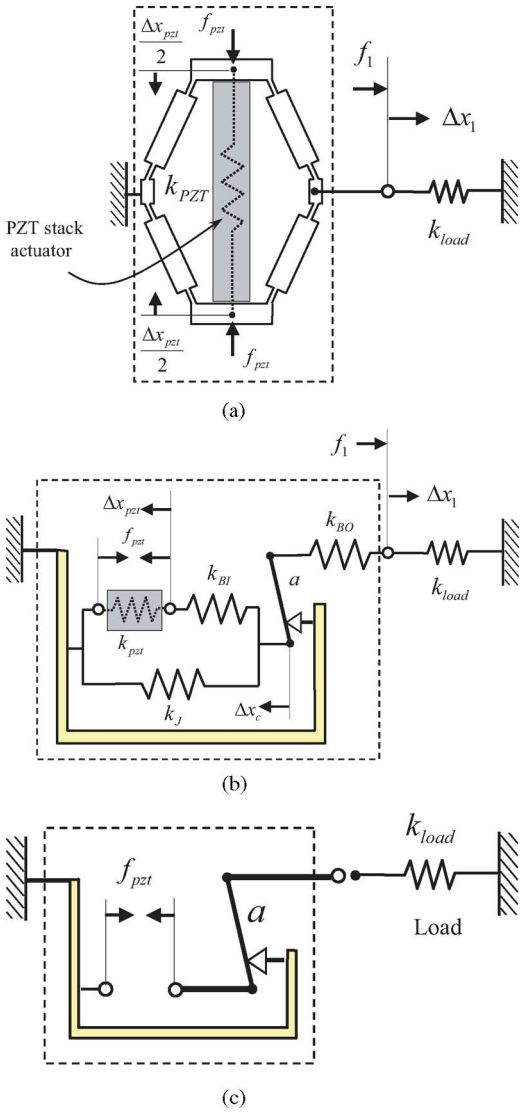


Fig. 10. Model of rhombus mechanism with flexibility. (a) Rhombus mechanism with structural flexibilities. (b) Proposed lumped parameter model. (c) Model of idealized rhombus ($k_{BI}, k_{BO} \to \infty, k_J \to 0$).

is a stiffness matrix. $f_I$ is the net force applied to the mechanism from the internal unit, and $f_O$ is the reaction force from the external load. Note that the stiffness matrix $\boldsymbol{S}$ is nonsingular, symmetric, and positive-definite; $s_1 > 0$, $s_2 > 0$, and $s_1 s_2 - s_3^2 > 0$. The symmetric nature of the stiffness matrix follows Castigliano's theorems. When the input port is connected to a PZT stack actuator producing force $f_{\rm PZT}$ with inherent stiffness $k_{\rm PZT}$ and the output port is connected to a load of stiffness $k_{\rm load}$, we have

$$f_I = f_{\rm PZT} - k_{\rm PZT}\Delta x_{\rm PZT} = s_1 \Delta x_{\rm PZT} + s_3 \Delta x_1 \tag{20}$$

$$f_O = -f_1 = -k_{\rm load}\Delta x_1 = s_3 \Delta x_{\rm PZT} + s_2 \Delta x_1. \tag{21}$$

Eliminating $\Delta x_{\rm PZT}$ from the aforementioned equations yields

$$f_{\rm PZT} = -\left(\frac{k_{\rm PZT}+s_1}{s_3}k_{\rm load} + \frac{s_2(k_{\rm PZT}+s_1)-s_3^2}{s_3}\right)\Delta x_1. \tag{22}$$

Defining

$$\tilde{f} \triangleq \frac{-s_3}{k_{\rm PZT}+s_1} f_{\rm PZT} \tag{23}$$

$$\tilde{k} \triangleq \frac{s_2(k_{\rm PZT}+s_1)-s_3^2}{k_{\rm PZT}+s_1} = \frac{s_2 k_{\rm PZT} + \det \boldsymbol{S}}{k_{\rm PZT}+s_1} > 0 \tag{24}$$

the aforementioned equation (22) reduces to

$$\tilde{f} = (k_{\rm load} + \tilde{k})\Delta x_1. \tag{25}$$

Force $\tilde{f}$ and stiffness $\tilde{k}$ represent the effective PZT force and the resultant stiffness of the PZT stack all viewed from the output port of the amplification mechanism.

A drawback with the two-port model representation is that it is hard to gain physical insights as to which elements degrade actuator performance and how to improve it through design. In the previous section, two distinct compliances were introduced, one in the admissible motion space and the other in the constrained space. To improve performance with respect to output force and displacement, the stiffness in the admissible motion space must be minimized, while the one in the constrained space must be maximized. To manifest these structural compliances, we propose a lumped parameter model shown in Fig. 10(b) with three spring elements $k_J$, $k_{BI}$, and $k_{BO}$ and one amplification leverage $a$. As the spring constants $k_{BI}$ and $k_{BO}$ tend to infinity, the system reduces to the one consisting of all rigid links, where the output $\Delta x_1$ is directly proportional to the input displacement $\Delta x_{\rm PZT}$. Stiffness $k_J$ impedes this rigid body motion, representing the stiffness in the admissible motion space. Elastic deformation at $k_{BI}$ and $k_{BO}$ represent deviation from the rigid body motion.

From Fig. 10(b)

$$f_{\rm PZT} + k_{BI}(\Delta x_c - \Delta x_{\rm PZT}) - k_{\rm PZT}\Delta x_{\rm PZT} = 0 \tag{26}$$

$$a\,k_{BO}(a\Delta x_c - \Delta x_1) + k_J \Delta x_c + k_{BI}(\Delta x_c - \Delta x_{\rm PZT}) = 0 \tag{27}$$

$$f_1 = k_{\rm load}\Delta x_1 = k_{BO}(a\Delta x_c - \Delta x_1) \tag{28}$$

where $\Delta x_c$ is the displacement at the connecting point between the leverage and springs; however, this point is virtual and $\Delta x_c$ does not correspond to a physical displacement. This model is applicable to a wide variety of "rhombus-type" amplification mechanisms including Moonies. See Appendix for more detail about the validation of the model and parameter calibration.

Consider the blocking force when the PZT stack actuator generates its maximum force $f_{\rm PZTmax}$ given as follows:

$$f_1^{\rm block} = \frac{a k_{BI} k_{BO}}{(a^2 k_{BI} k_{BO} + k_{BI} k_J) + k_{\rm PZT}(a^2 k_{BO} + k_J + k_{BI})} \times f_{\rm PZTmax}. \tag{29}$$

Similarly, the free-load displacement for this rhombus mechanism, where $k_{\rm load} \to 0$, is given by

$$\Delta x_1^{\rm free} = \frac{a k_{BI}}{k_{\rm PZT}(k_{BI}+k_J) + k_J k_{BI}} f_{\rm PZTmax}. \tag{30}$$

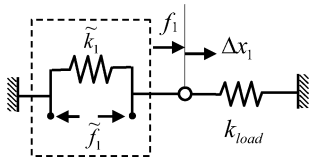


Fig. 11. Simplified representation of lumped-parameter model.

As addressed, these equations imply that the blocking force will be maximized by $k_{BI}, k_{BO} \to \infty$. Similarly, $k_J \to 0$ maximizes $\Delta x_1^{\text{free}}$.

The other advantage is that the three-spring model is able to represent the ideal rhombus shown in Fig. 9(a), as a special case as shown in Fig. 10(c). See (42) and confirm that the stiffness matrix $\boldsymbol{S}$ cannot be defined for both $k_{BI}, k_{BO} \to \infty$ and $k_J \to 0$. As described in Section V, the number of unknown parameters becomes four, as the rigid amplification leverage is explicitly included, which makes the calibration problem ill-posed; however, this amplification leverage is necessary to include the ideal case. In addition, three lumped springs are considered minimum to satisfy the input–output bidirectionality, which is a basic requirement of Castigliano's theorems.

### C. Model Simplification

From (26) to (28), the relationship between $f_{\text{PZT}}$ and $\Delta x_1$ is given by

$$\begin{aligned}(a\, k_{BI}k_{BO})f_{\text{PZT}} &= [k_{\text{load}}\{a^2 k_{BI}k_{BO} + k_{BI}k_J + k_{\text{PZT}}(a^2 k_{BO} + k_J + k_{BI})\} \\ &\quad + k_{BO}(k_{BI}k_J + k_{\text{PZT}}k_J + k_{BI}k_{\text{PZT}})]\Delta x_1. \end{aligned} \tag{31}$$

The aforementioned equation can be written as

$$\tilde{f}_1 = (k_{\text{load}} + \tilde{k}_1)\Delta x_1 \tag{32}$$

where

$$\tilde{k}_1 \triangleq \frac{k_{BO}(k_{BI}k_J + k_{\text{PZT}}k_J + k_{BI}k_{\text{PZT}})}{(a^2 k_{BI}k_{BO} + k_{BI}k_J) + k_{\text{PZT}}(a^2 k_{BO} + k_J + k_{BI})} \tag{33}$$

$$\tilde{f}_1 \triangleq \frac{a k_{BI}k_{BO}}{(a^2 k_{BI}k_{BO} + k_{BI}k_J) + k_{\text{PZT}}(a^2 k_{BO} + k_J + k_{BI})} \times f_{\text{PZT}}. \tag{34}$$

This implies that the proposed lumped parameter model shown in Fig. 10(b) can be further simplified to Fig. 11. Note that, the direction of $\tilde{f}_1$ is opposite to $f_{\text{PZT}}$ due to the amplification leverage. This simplified model has a similar form as in (25).

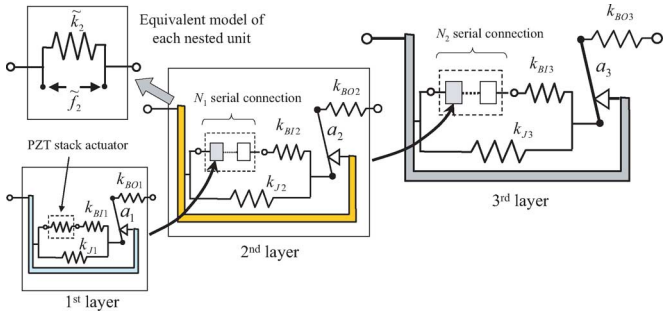


Fig. 12. Recursive formula for nested rhombus model.

As will be described in the following section, this simplification enables performance evaluation of complex nested mechanisms simply by nesting a simplified model of lower layers into a higher lumped parameter model. As a result, the performance of the overall mechanism such as aggregate displacement and force can be predicted in a recursive manner without developing a full FEM model [22] or solving continuum elastic equations [28]; parameter calibration at the layer-level is sufficient.

### D. Recursive Formula of Aggregate Force and Displacement of Flexible Nested Mechanisms

The goal of this section is to describe a recursive formula to obtain an equivalent model for a general nested mechanism. Fig. 12 shows a nested rhombus structure. As addressed in the previous sections, each nested layer can be represented by its equivalent model, which enables us to describe the force–displacement property for the nested structure in an iterative manner. Let $K$ be the number of nesting layers. Also, let $k_{Jk}$, $k_{BIk}$, $k_{BOk}$, $N_k$ be the joint compliance, beam compliances, and the number of serial connection for the $k$th $(k = 1, \ldots K)$ layer. This mechanism involves $N_{K-1}, N_{K-2}, \ldots, N_1$ PZT stack actuators.

By applying (33) and (34), the equivalent model for the $k$th layer can be represented by (35) and (36), shown at the bottom of this page, where $\tilde{f}_{k-1}^i$ is the equivalent force of the $i$th unit in the $(k-1)$th layer. Recall that $\tilde{f}_k$ is proportional to the average of the entire forces at the $(k-1)$th layer as described in Section III-A.

Assume that all actuators in the $(k-1)$th layer are controlled in a binary manner [4], i.e., $V_{k-1}^i = \{V_{\max}\ (\text{ON}),\ 0\ (\text{OFF})\}$. Also assume that all units are uniform and each unit generates $\tilde{f}_{k-1}^{\text{block}}$ as its blocking force. Therefore, when $n$ units out of $N_{k-1}$

$$\tilde{k}_k = \frac{k_{BOk}(k_{BIk}k_{Jk} + \frac{\tilde{k}_{k-1}}{N_{k-1}}k_{Jk} + k_{BIk}\frac{\tilde{k}_{k-1}}{N_{k-1}})}{(a_k^2 k_{BIk}k_{BOk} + k_{BIk}k_{Jk}) + \frac{\tilde{k}_{k-1}}{N_{k-1}}(a_k^2 k_{BOk} + k_{Jk} + k_{BIk})} \tag{35}$$

$$\tilde{f}_k = \frac{a_k k_{BIk}k_{BOk}}{(a_k^2 k_{BIk}k_{BOk} + k_{BIk}k_{Jk}) + \frac{\tilde{k}_{k-1}}{N_{k-1}}(a_k^2 k_{BOk} + k_{Jk} + k_{BIk})} \frac{1}{N_{k-1}} \sum_{i=1}^{N_{k-1}} \tilde{f}_{k-1}^i \tag{36}$$

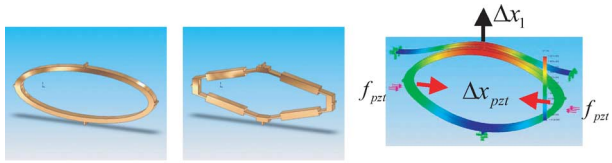


Fig. 13. Example of amplification mechanisms. (a) Structure 1. (b) Structure 2. (c) Dispalcement when connected to a fixed beam.

actuators are ON, the last term of (36) can be replaced as

$$\frac{1}{N_{k-1}}\sum_{i=1}^{N_{k-1}} \tilde{f}_{k-1}^{i} \rightarrow \frac{n}{N_{k-1}} \tilde{f}_{k-1}^{\text{block}}. \tag{37}$$

The free-load displacement changes accordingly. Both the aggregate free-load displacement and the blocking force are proportional to the number of ON units.

## V. Verification and Calibration of Three-Spring Lumped-Parameter Model

The validity of the proposed lumped parameter model is confirmed by FEM. Consider the two amplification mechanisms shown in Fig. 13 for example. The size of the both mechanisms is: 40 mm (length, actuation direction) × 96 mm (width) × 5 mm (thickness). Brass (Young's modulus = 100.0 GPa) is used. The four structural lumped parameters, i.e., $a$, $k_{BI}$, $k_{BO}$, and $k_J$ are calibrated by the displacements and forces from two different conditions; one case is "blocked case" where the output displacement is totally constrained (or letting $k_{\text{load}} \rightarrow \infty$), and the other one is "free-load case" (or letting $k_{\text{load}} = 0$).

By applying an input force, $f_{\text{PZT}}$, $\Delta x_{\text{PZT}}^{\text{block}}$ and $f_1^{\text{block}}$ are measured for the blocked case, and $\Delta x_{\text{PZT}}^{\text{free}}$ and $\Delta x_1^{\text{free}}$ are measured for the free-load case. From (26) to (28), we have

$$\frac{f_{\text{PZT}}^{\text{block}}}{\Delta x_{\text{PZT}}^{\text{block}}} = \frac{a^2 k_{BI} k_{BO} + k_J k_{BI}}{a^2 k_{BO} + k_J + k_{BI}} \triangleq X_1 \tag{38}$$

$$\frac{f_1^{\text{block}}}{\Delta x_{\text{PZT}}^{\text{block}}} = \frac{a k_{BI} k_{BO}}{a^2 k_{BO} + k_J + k_{BI}} \triangleq X_2 \tag{39}$$

$$\frac{\Delta x_1^{\text{free}}}{\Delta x_{\text{PZT}}^{\text{free}}} = \frac{a\, k_{BI}}{k_J + k_{BI}} \triangleq X_3 \tag{40}$$

$$\frac{f_{\text{PZT}}^{\text{free}}}{\Delta x_1^{\text{free}}} = \frac{k_J}{a} \triangleq X_4. \tag{41}$$

Note that, the actual number of independent equations described here is three, which can be confirmed by $X_1 = X_3(X_2 + X_4)$. This implies that the calibration of the four structural parameters, $[a, k_{BI}, k_{BO}, k_J]$, is an ill-posed problem. This can be confirmed by the two-port model representation in (19). The stiffness matrix $\boldsymbol{S}$ is generally given as

$$\boldsymbol{S} = \begin{bmatrix} X_1 & -X_2 \\ -X_2 & \frac{X_3}{X_2} \end{bmatrix}. \tag{42}$$

Recall $\boldsymbol{S} = \boldsymbol{S}^T$ and it fully represents the relation between the displacements and forces. Therefore, the number of independent elements is three by calibrating $\boldsymbol{S}$. Unlike the ideal rhombus mechanism consisting of all rigid links, the displacement amplification gain $a$ cannot be defined uniquely as long as the stiffness in the constrained space is finite, i.e., $k_J > 0$. Note that, the choice of $a$ does not change $\boldsymbol{S}$ or the characteristics of the estimated model; however, a nominal gain $\hat{a}$ should be determined to have a physically feasible lumped parameter model, that is, $k_{BI}, k_{BO}, k_J > 0$. One way of determining $\hat{a}$ is based on free-displacement characteristics and kinematic characteristics of the structure such as the angle of the oblique beam $\theta$, i.e., $X_3 < \hat{a} < \cot\theta$, to satisfy the requirement. $X_3$ can be assumed as a lower bound of $\hat{a}$ since $X_3$ is always lower than the actual $a$ if $k_J$ is positive. In addition, $\cot\theta$ can be assumed as an upper bound of $\hat{a}$ since this gain is realized only when $k_J = 0$. The following steps estimate the remaining parameters: $\hat{k}_J = \hat{a}\, X_4$, $\hat{k}_{BI} = X_3 \hat{k}_J / \hat{a} - X_3$, and $\hat{k}_{BO} = (\hat{k}_{BI} + \hat{k}_J) X_2 / \hat{a} \hat{k}_{BI} - \hat{a}^2 X_2$.

TABLE I
Observed Values from FEM

| | Structure 1 | Structure 2 |
|---|---|---|
| $\Delta x_1^{free}$ [m] (@$f_{pzt}$=10) | 1.95e-05 | 2.61e-04 |
| $f_1^{block}$ [N] (@$f_{pzt}$=10) | 2.73 | 2.51 |
| $X_1$ | 6.64e+06 | 1.25e+07 |
| $X_2$ | 1.81e+06 | 3.14e+06 |
| $X_3$ | 2.88 | 3.89 |
| $X_4$ | 5.13e+05 | 3.84e+04 |

TABLE II
Estimated Lumped Parameters

| | Structure 1 | Structure 2 |
|---|---|---|
| $\hat{a}$ | 3.2 | 3.9 |
| $\hat{k}_J$ [N/m] | 1.64e+06 | 1.50e+05 |
| $\hat{k}_{BI}$ [N/m] | 1.46e+07 | 4.25e+07 |
| $\hat{k}_{BO}$ [N/m] | 1.05e+06 | 1.13e+06 |
| $\sigma_{max}$ [N/m$^2$] | 5.35e+06 | 2.75e+07 |

Table I shows the observed values from FEM when applying $f_{\text{PZT}}$ =10 N. The structural lumped parameters are calculated as shown in Table II. The nominal amplification gains are determined accordingly based on the observed $X_3$s and kinematic characteristics to keep all spring constants positive. As shown in Table I, Structure 2 provides approximately 13 times larger free-load displacement than Structure 1, while the blocking forces of the two structures are almost the same magnitude. This observation suggests that Structure 2 has a more favorable structure than Structure 1 as an amplification mechanism. This can be explained based on the estimated lumped parameters: The effective stiffness in the constrained space $\bar{k_B}$ viewed from the input port is calculated as

$$\bar{k_B} \triangleq \frac{1}{(1/k_{BI}) + (1/a^2 k_{BO})}. \tag{43}$$

This expression gives $\bar{k_B}$ =6.18e+06 for Structure 1 and $\bar{k_B}$ =1.23e+07 for Structure 2. As a result, Structure 2 has a smaller stiffness in the admissible space $k_J$ and a larger stiffness in the constrained space $\bar{k_B}$ compared with Structure 1. Although Structure 2 provides relatively good performances, it could also have problems in development due to its complex

TABLE III
ESTIMATED DISPLACEMENTS

| $t$ [mm] | Disp. [$\mu$m] | Structure 1 FEM | Structure 1 Model | Structure 1 Error [%] | Structure 2 FEM | Structure 2 Model | Structure 2 Error [%] |
|---|---|---|---|---|---|---|---|
| 1 | $\Delta xpzt$ | 6.48 | 6.49 | 0.035 | 36.76 | 37.20 | 1.184 |
| | $\Delta x_1$ | 18.40 | 18.42 | 0.172 | 141.5 | 143.1 | 1.163 |
| 2 | $\Delta xpzt$ | 5.10 | 5.11 | 0.187 | 9.47 | 9.57 | 1.098 |
| | $\Delta x_1$ | 13.28 | 13.34 | 0.467 | 34.09 | 34.46 | 1.098 |
| 3 | $\Delta xpzt$ | 3.56 | 3.56 | 0.051 | 3.65 | 3.67 | 0.492 |
| | $\Delta x_1$ | 7.61 | 7.63 | 0.301 | 11.23 | 11.30 | 0.267 |
| Ave. [%] | | | | 0.202 | | | 0.884 |

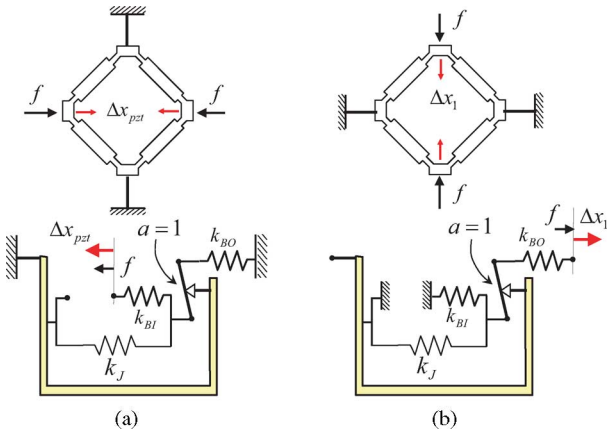


Fig. 14. Requirement of input-output bidirectionality. (a) Output constrained. (b) Input-output constrained.

shape and in strength due to stress concentration at thin sections having large deformation. Maximum stress when producing the free-load displacement is shown in Table II.

The validity of the calibrated models is confirmed by examining $\Delta x_{\rm PZT}$ and $\Delta x_1$ when connecting the mechanism to a spring load realized by a fixed beam shown in Fig. 13(c). The length of the beam is $L$ =100 mm and brass is used as material. There is a small protrusion on the top of the actuator so that the amplification mechanism and the fixed beam are assumed to be in point contact. Three different thicknesses, from 1 to 3 mm, are used to vary the stiffness. Table III shows the comparison of the estimated displacements from the proposed lumped parameter model and the true values from FEM analysis. As can be observed in the table, the estimated values agree well with the true values, confirming the validity of the model.

Consider two constrained cases as shown in Fig. 14(a) and (b) to confirm the necessity of three lumped springs. For simplicity, the amplification mechanism is designed to have a square shape resulting in $a = 1$. $\Delta x_1 = \Delta x_{\rm PZT}$ must hold for the displacements when applying the same magnitude of force $f$, which is a basic requirement of Castigliano's theorems. By using the proposed lumped parameter model, these constrained cases are represented in the figures shortly. The condition $\Delta x_1 = \Delta x_{\rm PZT}$ is satisfied if $k_{BI} = k_{BO}$. This can also be confirmed in (42) where the off-diagonal elements are the same. As described in Section V, this lumped parameter model has a redundancy in parameter calibration; however, three spring elements are minimally required to satisfy this condition.

TABLE IV
CHARACTERISTICS OF THE APA50XS ACTUATOR [23] FOR THE FIRST LAYER (DEFINITION OF THE DIMENSIONS HAS BEEN MODIFIED)

| | |
|---|---|
| Displacement | 80 [$\mu$m] |
| Blocking Force $\tilde{f}_1^{block}$ | 18.0 [N] |
| Stiffness $\tilde{k}_1$ | 0.225 [N/$\mu$m] |
| Voltage range | -20 – 150 [V] |
| Length (output actuation direction) | 4.7 [mm] |
| Width (pzt stack actuation direction) | 12.8 [mm] |
| Height | 9.0 [mm] |
| Mass | 2.0 [g] |

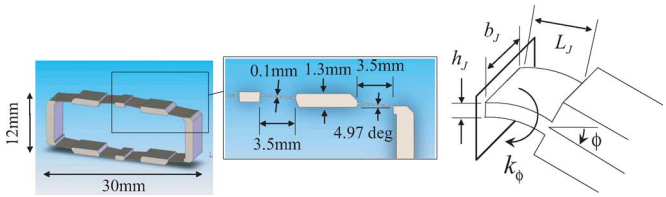


Fig. 15. Design of rhombus mechanism for the second layer.

## VI. PROTOTYPE ACTUATOR

### A. Mechanical Design of Rhombus Mechanism

A prototype nested actuator with over 20% effective strain is designed based on the structural compliance analysis. Consider a nested structure with two amplification layers as shown in Fig. 3. The APA50XS "Moonie" piezoelectric actuators developed by Cedrat Inc. [23] are adopted for the first layer. According to the preliminary design in Section II, over 20% of effective strain can be obtained by a two-layer mechanism; $K = 2$ and $\alpha = 15$. By stacking six APA50XS actuators for the first layer, i.e., $N_1 = 6$, this large strain may be achieved with a proper design of the second layer. From Table IV, we have $\tilde{k}_1 = 0.225 \times 10^6$ N/m, and $\tilde{f}_1^{\rm block} = 18.0$ N for the first layer units. The remainder of this section focuses on the design of the second-layer rhombus mechanism. From (35) and (36), we obtain an equivalent model for the second layer by substituting (33) and (34), which provide a design guideline in terms of $k_{BI2}$, $k_{BO2}$, and $k_{J2}$ for the target effective strain, i.e., 20%.

As described in the previous section, the stiffness in the admissible space, i.e., $k_{J2}$, must be minimized. The compliant joint may be represented as shown in Fig. 15. The rotational stiffness of this structure is given by $k_\phi = Eb_J h_J^3/12L_J$, where $E$ is Young's modulus of the material. In order to reduce this stiffness, either the width $b_J$ or thickness $h_J$ must be reduced, or length of the gap $L_J$ must be increased. Note that, the reduction of $h_J$ is the most effective for reducing $k_{J2}$ since it is proportional to $h_J^3$; however, the thickness must be carefully determined considering manufacturing process. The maximum stress must be lower than the yield stress of material. In addition, in order to increase the stiffness in the constrained space, i.e., $k_{BI2}$ and $k_{BO2}$, the oblique beam need to have a sufficient thickness except the thin part for the compliant joint.

Fig. 15 shows the designed rhombus mechanism for the second layer. Phosphor bronze (C54400, H08) is used for the material. The length of the mechanism in actuation direction is 12 mm, and the width is 30 mm. The thickness of 0.1 mm is

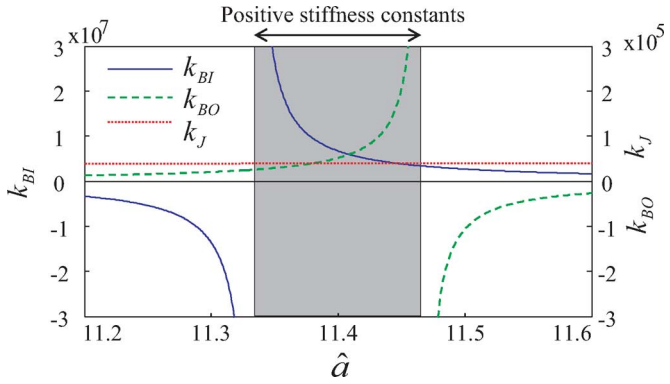


Fig. 16. Choice of $\hat{a}$ for positive spring constants.

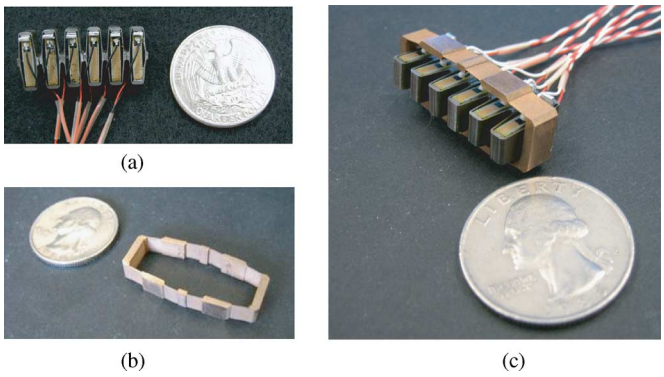


Fig. 17. Prototype actuator: six CEDRAT actuators are used for the first layer. (a) Connected first layer units. (b) Second layer amplification mechanism. (c) Assembled actuator.

given to $h_J$ for electrical discharge machining. The thickness of 1.3 mm is given to the oblique beams for sufficient stiffness. The oblique angle of the beams is $4.97°$ that gives the displacement amplification ratio of 11.5, assuming the mechanism is ideal.

For the second layer mechanism shown in Fig. 15, $X_1 = 3.39 \times 10^6$, $X_2 = 2.95 \times 10^5$, $X_3 = 11.33$, and $X_4 = 3.50 \times 10^3$ are obtained from FEM analysis. The range of $a_2$ that makes all spring constants positive is shown in Fig. 16. Finally, $\hat{a}_2 = 11.4$ is chosen, which is between $X_3$ and $\cot\theta$ (=11.5). Finally, the parameters for the lumped parameter model are calculated as $\hat{k}_{BI2} = 6.72 \times 10^6$ N/m, $\hat{k}_{BO2} = 5.21 \times 10^4$ N/m, $\hat{k}_{J2} = 3.98 \times 10^4$ N/m by determining the amplification gain as $\hat{a}_2 = 11.4$. The analysis using the lumped parameter model predicts that the maximum free-load displacement is 2.64 mm, which is equivalent to 22% effective strain. Also, the maximum blocking force is 1.56 N.

### B. Development and Performance Evaluation

Fig. 17(a) shows the developed rhombus mechanism for the second layer and (b) shows the assembled actuator with six first-layer units. The second layer mechanism weighs approximately 3 g, resulting in the total weight of 15 g. The connected first-layer units were inserted in the second layer mechanism and the both ends were manually bonded to the inside walls. Note that, we noticed that the tolerances on the interfaces were important

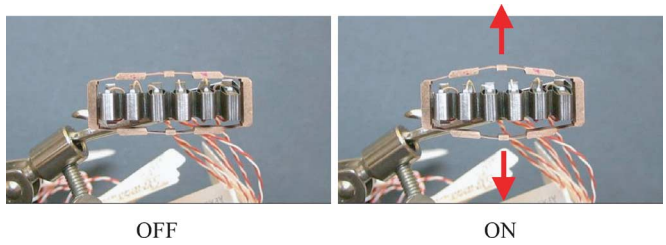


Fig. 18. Free-load displacement when all of the six first-layer actuators are ON.

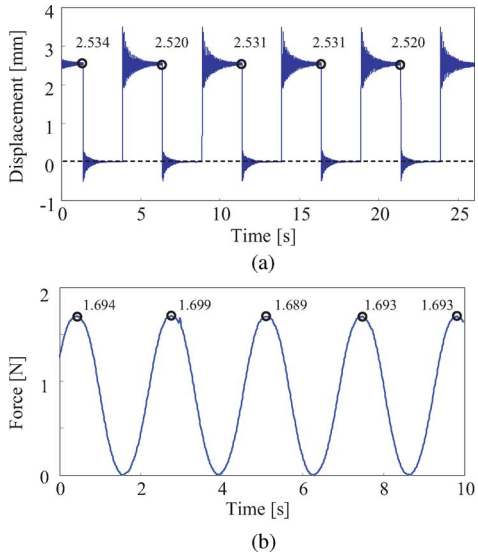


Fig. 19. Experimental result. (a) Free-load displacement (step response). (b) Blocking-force (sinusoidal wave input).

for satisfactory actuator performances. Fig. 18 shows snapshots of free-load displacement where two rhombus mechanisms are connected in series. This actuator extends since the first layer units are contractive.

The performance of this prototype is evaluated by measuring free-load displacement and blocking force. Fig. 19(a) shows the maximum free-load displacement measured using a laser displacement sensor (Micro-Epsilon optoNCDT 1401) when all six units are ON by applying 150 V actuation voltage. The measured displacement is 2.53 mm that is equivalent to 21.1% effective strain. Fig. 19(b) shows the blocking force where a sinusoidal wave input ranging from 0 to 150 V is applied. The maximum blocking force measured using a compact load cell (Transducer Techniques MLP) is 1.69 N. As shown in Table V, the experimental values by using the lumped parameter model agree well with the estimated values, which confirm the validity of the approach.

Fig. 20 shows the aggregate displacements when ON–OFF control is applied to the internal six units by applying a constant actuation voltage when ON. For convenience, the measured displacements are normalized by the maximum displacement when all 6 units are turned on. As described in Sections III-A, and IV-D, the distribution of the ON units in a layer does not theoretically affect on the aggregate displacement if an amplification mechanism encloses serially connected internal units.

TABLE V
COMPARISON BETWEEN IDEALIZED MODEL, PROPOSED LUMPED PARAMETER MODEL, AND EXPERIMENTAL MEASUREMENT

| | Analysis Idealized model | Analysis Lumped model | Experiment |
|---|---|---|---|
| Effective strain | 23.9 [%] | 22.0 [%] | 21 [%] |
| Free displacement | 2.8 [mm] | 2.64 [mm] | 2.53 [mm] (std $5.9 \times 10^{-3}$) |
| Blocking force | 15.1 [N] | 1.56 [N] | 1.69 [N] (std $3.25 \times 10^{-3}$) |

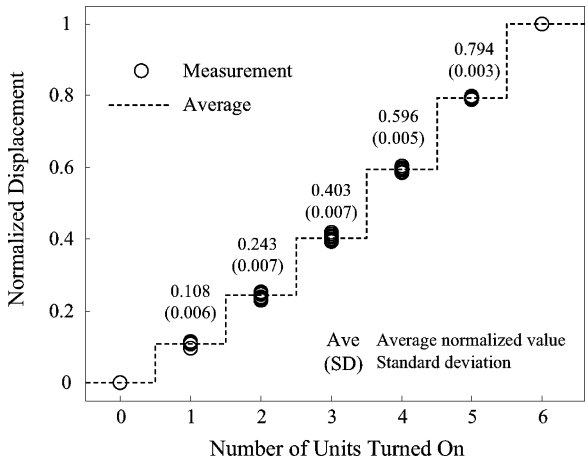


Fig. 20. Binary ON-OFF control experiment.

As can be observed in Fig. 20, the measured displacement is not largely affected by the combination of ON units. For example, there are 20 ($=_6C_3$) combinations when the number of ON units is 3; however, the standard variation is at most 0.007, showing a sufficient repeatability. Another observation is that the increment of the displacement is not uniform, which is considered due to the nonlinearity of (1). In Section II-A, we have neglected this issue for simplicity; however, this characteristic should be further reflected to the design and control if rhombus mechanisms are used for creating large strain.

The comparison between Figs. 5 and 19 suggests that the aggregated force has been considerably attenuated, while the aggregated displacement or strain is as large as predicted by the idealized analysis. Note again that the result in Fig. 5 will never be achieved unless completely rigid beams and purely rotational joints without play are utilized. One of the difficulties in mechanical design is that physical structural parameters are intricately related to lumped parameters. For example, the increase of the gap $L_J$ in Fig. 15 contributes to reducing the joint stiffness but it also reduces the beam stiffness by having a long thin gap in the longitudinal direction. This gap may be reduced if the design focus is more on producing a larger blocking force.

### C. Modular Design of Cellular Actuators

The authors have proposed a new control method to control vast number of cellular units for the cellular actuator concept inspired by the muscle behavior [3]–[5]. Instead of wiring many control lines to each individual cell, each cellular actuator has a stochastic local control unit that receives the broadcasted signal from the central control unit, and turns its state in a simple ON–OFF manner as described in Section III-A. A $2 \times 2$ array structure using polyvinylidenefluoride (PVdF) film actuators has been fabricated that produced 1.2 mm free displacement and 5.5 mN blocking force from 120 mm $\times$ 22 mm footprint [20], whose force may be insufficient to drive macro-size robots. Fig. 21 shows two example configurations, where cells are connected in series (stack) and in parallel (bundle). A wide variety of sizes and shapes is configurable using the designed actuator as a building-block. For example, the configuration shown in the right is expected to produce 11.8 N (1.67 N $\times$ 7 bundles) of blocking force and 15.2 mm (2.53 mm $\times$ 6 stacks) of free displacement if the developed units are applied. The macro actuator array in the figure corresponds to a single muscle, and each of the prototype units (cells) corresponds to Sarcomere known to be controlled in an ON–OFF manner. For example, a pair of the actuator arrays will be attached to a link mechanism in an antagonistic arrangement.

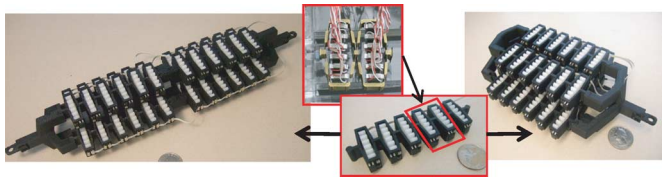

Fig. 21. Modularity of cellular actuators: mock-up cellular actuators with 12 stacks and 4 bundles (left) and 6 stacks and 7 bundles (right).

## VII. CONCLUSION AND FUTURE WORK

This paper has presented a nested rhombus multilayer mechanism for PZT actuators. The idealized analysis has been given for fundamental design of the nested structure. Through kinematic and static analysis, this paper has addressed how the output force and displacement are attenuated by the structural compliances involved in the strain amplification mechanism. A lumped parameter model has been proposed to quantify the performance degradation. A prototype-nested PZT cellular actuator that weighs only 15 g has produced 21% effective strain (2.53 mm displacement from 12 mm actuator length and 30 mm width) and 1.69 N blocking force. A modular design concept has been presented for building reconfigurable cellular actuators with matched stroke and force requirements. Future work includes: 1) nonlinear and dynamic modeling such as frequency response; 2) analysis of a closed kinematic chain formed by serial-parallel mixed configuration; 3) design optimization and efficiency analysis; 4) application to practical systems such as robot hands and rehabilitation robots. Especially, dynamic analysis is important for high-speed actuation. Based on our preliminary work [25], the dynamics modeling will be discussed in our future publication. The future work also includes 5) investigation of manufacturing aspects for accuracy improvement and future cost reduction since the number of actuators as well as the complexity increase as the number of layer increases.

## REFERENCES


[1] J. Ueda, T. Secord, and H. Asada, "Static lumped parameter model for nested PZT cellular actuators with exponential strain amplification mechanisms," in *Proc. IEEE Int. Conf. Robot. Autom. (ICRA 2008)*, pp. 3582–3587.

[2] J. Ueda, T. Secord, and H. Asada, "Piezoelectric cellular actuators using nested rhombus multilayer mechanisms," presented at the 1st Annu. Dyn. Syst. Control Conf. (DSCC 2008), Ann Arbor, MI.

[3] J. Ueda, L. Odhnar, and H. Asada, "A broadcast-probability approach to the control of vast dof cellular actuators," in *Proc. IEEE Int. Conf. Robot. Autom. (ICRA 2006)*, May 15–19, pp. 1456–1461.

[4] J. Ueda, L. Odhner, and H.˜H. Asada, "Broadcast feedback of stochastic cellular actuators inspired by biological muscle control," *Int. J. Robot. Res.*, vol. 26, no. 11–12, pp. 1251–1265, 2007.

[5] J. Ueda, L. Odhner, and H. H. Asada, "Broadcast feedback for stochastic cellular actuator systems consisting of nonuniform actuator units," in *Proc. IEEE Int. Conf. Robot. Autom. (ICRA 2007)*, Apr. 10–14, pp. 642–647.

[6] J. Ueda, M. Matsugashita, R. Oya, and T. Ogasawara, "Control of muscle force during exercise using a musculoskeletal-exoskeletal integrated human model," in *Proc. Exp. Robot.*, 2008, pp. 143–152.

[7] F. H. Martini and E. F. Bartholomew (2006, Jan. 31). *Essentials of Anatomy & Physiology* (4th ed.). Benjamin Cummings. [Online]. Available: http://amazon.com/o/ASIN/0805373039/

[8] B. Selden, K. Cho, and H. H. Asada, "Segmented shape memory alloy actuators using hysteresis loop control," *Smart Mater. Struct.*, vol. 15, no. 2, pp. 642–652, 2006.

[9] R. Newnham, A. Dogan, Q. Xu, K. Onitsuka, J. Tressler, and S. Yoshikawa, "Flextensional moonie actuators," in *Proc. IEEE Ultrason. Symp.*, Oct. 31–Nov. 3, 1993, vol. 1, pp. 509–513.

[10] A. Dogan, Q. Xu, K. Onitsuka, S. Yoshikawa, K. Uchino, and R. Newnham, "High displacement ceramic metal composite actuators (moonies)," *Ferroelectrics*, vol. 156, no. 1, pp. 1–6, 1994.

[11] G. Haertling, "Rainbow ceramics- A new type of ultra-high-displacement actuator," *Amer. Ceramic Soc. Bull.*, vol. 73, no. 1, pp. 93–96, 1994.

[12] A. Moskalik and D. Brei, "Quasi-static behavior of individual C-block piezoelectric actuators," *J. Intell. Mater. Syst. Struct.*, vol. 8, no. 7, pp. 571–587, 1997.

[13] K. Uchino, *Piezoelectric Actuators and Ultrasonic Motors*. Norwell, MA: Kluwer, 1997.

[14] A. Dogan, K. Uchino, and R. Newnham, "Composite piezoelectric transducer with truncated conical endcaps "cymbal"," *IEEE Trans. Ultrason., Ferroelectr. Freq. Control*, vol. 44, no. 3, pp. 597–605, May 1997.

[15] I. Fukui, T. Yano, and T. Hamatsuki, "Lever actuator comprising a longitudinal-effect electroexpansive transducer and designed to prevent actuation from degrading the actuator," U.S. Patent 4 435 666, Mar. 6, 1984.

[16] P. Janker, M. Christmann, F. Hermle, T. Lorkowski, and S. Storm, "Mechatronics using piezoelectric actuators," *J. Eur. Ceramics Soc.*, vol. 19, no. 6, pp. 1127–1131, 1999.

[17] C. Niezrecki, D. Brei, S. Balakrishnan, and A. Moskalik, "Piezoelectric actuation: State of the art," *Shock Vibration Dig.*, vol. 33, no. 4, pp. 269–280, 2001.

[18] K. Seffen and E. Toews, "Hyperhelical actuators: Coils and coiled-coils," in *Proc. 45th AIAA/ASME/ASCE/AHS/ASC Struct., Struct. Dyn. Mater. Conf.*, Apr. 2004, pp. 19–22.

[19] N. Conway, Z. Traina, and S. Kim, "A strain amplifying piezoelectric MEMS actuator," *J. Micromech. Microengineering*, vol. 17, no. 4, pp. 781–787, 2007.

[20] J. Ervin and D. Brei, "Recurve piezoelectric-strain-amplifying actuator architecture," *IEEE/ASME Trans. Mechatronics*, vol. 3, no. 4, pp. 293–301, Dec. 1998.

[21] R. MacGregor, "Shape memory alloy actuators and control methods," U.S. Patent 6 574 958, Jun. 10, 2003.

[22] E. Silva, S. Nishiwaki, and N. Kikuchi, "Topology optimization design of flextensional actuators," *IEEE Trans. Ultrason., Ferroelectr. Freq. Control*, vol. 47, no. 3, pp. 657–671, May 2000.

[23] CEDRAT Piezo Products Catalogue Version 3.2, CEDRAT Inc. (2007). [Online]. Available: http://www.cedrat.com

[24] A. Mezheritsky, "Invariants of electromechanical coupling coefficients in piezoceramics," *IEEE Trans. Ultrason., Ferroelectr. Freq. Control*, vol. 50, no. 12, pp. 1742–1751, Dec. 2003.

[25] T. Secord, J. Ueda, and H. Asada, "Dynamic analysis of a high-bandwidth, large-strain, pzt cellular muscle actuator with layered strain amplification," in *Proc. IEEE Int. Conf. Robot. Autom. (ICRA 2008)*, pp. 761–766.

[26] I. Chopra, "Review of state of art of smart structures and integrated systems," *AIAA J.*, vol. 40, no. 11, pp. 2145–2187, 2002.

[27] H. Asada and J. Slotine, *Robot Analysis and Control*. New York: Wiley, 1986, ch. 7.

[28] W. Shih, W. Shih, and I. Aksay, "Scaling analysis for the axial displacement and pressure of flextensional transducers," *J. Amer. Ceramic Soc.*, vol. 80, no. 5, pp. 1073–1078, 1997.


**Jun Ueda** (M'01) received the B.S., M.S., and Ph.D. degrees from Kyoto University, Kyoto, Japan, in 1994, 1996, and 2002, respectively, all in mechanical engineering.

From 1996 to 2000, he was a Research Engineer with the Advanced Technology Research and Development Center, Mitsubishi Electric Corporation, Hyogo, Japan. From 2002 to 2008, he was an Assistant Professor in the Graduate School of Information Science, Nara Institute of Science and Technology, Nara, Japan. From 2005 to 2008, he was a Visiting Scholar and Lecturer in the Department of Mechanical Engineering, Massachusetts Institute of Technology, Cambridge. Since 2008, he has been with the George W. Woodruff School of Mechanical Engineering, Georgia Institute of Technology, as an Assistant Professor. His current research interests include vibration control, robust control, mechanical design, and biologically inspired robotics.

Dr. Ueda is a corecipient of the 2009 IEEE Robotics and Automation Society Early Academic Career Award.

**Thomas W. Secord** received the B.S. degree from the University of Minnesota, Minneapolis, in 2005, and the M.S. degree from the Massachusetts Institute of Technology, Cambridge, in 2007, both in mechanical engineering. He is currently working toward the Ph.D. degree in the Department of Mechanical Engineering, Massachusetts Institute of Technology.

His current research interests include robotics and control, mechatronics, artificial muscles, and actuator systems using smart materials.

**H. Harry Asada** (M'06) received the B.S., M.S., and Ph.D. degrees in precision engineering in 1973, 1975, and 1979, respectively, all from Kyoto University, Kyoto, Japan, where he specialized in robotics, biological engineering, and system dynamics and control.

He is currently the Ford Professor of Mechanical Engineering and Director of the Brit and Alex d'Arbeloff Laboratory for Information Systems and Technology, Department of Mechanical Engineering, Massachusetts Institute of Technology, Cambridge. His research interests include stochastic control, cellular actuators, underactuated robots, wearable health monitoring, and modeling and control of angiogenesis cell migration.

Dr. Asada is a Fellow of the American Society of Mechanical Engineers (ASME). He received Best Paper Awards at the IEEE International Conferences on Robotics and Automation in 1993, 1997, and 1999, the O. Hugo Schuck Best Paper Award from the American Control Council in 1985, Best Journal Paper Awards from the Society of Instrument and Control Engineers in 1979, 1984, and 1990, the Advanced Robotics Best Journal Paper Award in 2002, and the Dynamic Systems and Control Outstanding Researcher Award from the ASME in 1998.